Forced Imbibition and Uncertainty Modelling using the Morphological Method

Pit Arnold[1,*], *Mario* Dragovits[1], *Sven* Linden[2], *Fatime* Zekiri[3], and *Holger* Ott[1,†]

[1]Montanuniversität Leoben, Chair of Reservoir Engineering, 8700 Leoben, Austria
[2]Math2Market GmbH, 67655 Kaiserslautern, Germany
[3]OMV E&P GmbH, 1020 Vienna, Austria

Abstract. The morphological approach is a computationally attractive method for calculating relative permeability and capillary pressure saturation functions. In the workflow, morphological operations are used to calculate the fluid phase distribution in the pore space of a digital twin. Once the pore space is occupied, the fluid-phase conductivity and thus the relative permeability can be calculated by direct flow simulations on the phase occupied pore space. It therefore combines computational advantages that are used in pore network modeling with direct flow simulations on the digital twin. While the morphological operations conceptually correctly describe the primary drainage process, the imbibition process is described less obviously. So far, the method has delivered good results for drainage, but showed limitations in terms of imbibition processes and uncertainty modeling. In this work, we implement contact angle distributions in a deterministic and stochastic way in the approach. With this, we extend the simulated saturation range from purely spontaneous to forced imbibition, resulting in a full range imbibition relative permeability. Furthermore, by introducing stochastic contact angle distributions, different fluid phase distributions are obtained which allow for an uncertainty analysis. To verify the simulation results, we check (a) whether the simulation results agree with experience from SCAL measurements, and (b) compare the morphologically derived results and experimentally determined. Due to the newly introduced modifications, the imbibition process now behaves as physically expected and is in better agreement with experimental data compared to earlier studies.

1 Introduction

Digital Rock Physics (DRP) becomes increasingly attractive for computing multi-phase flow properties. Compared to classical Special Core Analysis (SCAL) experiments, DRP appears as less time and labor intensive, and hence as cost competitive. Furthermore, just small rock samples are required and therefore DR analysis can be applied to situations in which there are no suitable SCAL samples available.
DRP may be categorized in full physics models and reduced models. Full physics models provide deep insights in displacement physics, yet are typically computationally expensive and therefore possess limited use for upstream developments [1–3]. Methods such as Lattice Boltzmann are able to model the actual visco-capillary effects on the pore scale and therefore can reproduce experimental displacement results also outside capillary limits [4]. Yet their limitation lies within the possibility to vary petrophysical parameters such as the wettability of a system, as the simulations are highly time consuming.
Reduced models on the other hand are often computationally attractive, allowing for a larger number of simulations and hence for uncertainty analysis. Prominent examples are pore network models (PNM) which handle displacement physics in a rule-based fashion on idealized pore networks. The phase conductivities are computed by solving simplified analytical solutions rather than the underlying differential equations [5–7]. In PNM, the idealized pore networks are extracted by calculating the skeleton of the network, pore volumes and pore throat sizes from digital rock structures, with different authors using different algorithms [8–11]. All these algorithms are based on morphological operations.

The morphological method (MM), as presented in the following, makes use of morphological operations to calculate the fluid phase distribution directly in the digital twin, rather than to extract an idealized network. With this, the MM is bridging between both worlds; it makes use morphological operations to populate the as-measured pore space with the fluid phases, and solves the Navier-Stokes equation directly on the pore space to simulate effective permeability.
The morphological operations are applied in a rule-based, quasi-static manner, so that no time scale is associated with the displacement process. Since they are applied to the pore structure, the modelled displacement processes refer to a capillary-dominated flow – viscous processes are not considered. However, the fact that the displacement processes are purely calculated on basis of image processing makes the MM very time-competitive.
When simulating drainage processes, liquid invasion is controlled by the dilation of the mineral phase of the digital twin; pore throats are then identified and connectivity to

* Corresponding author: pit.arnold@unileoben.ac.at, †holger.ott@unileoben.ac.at

neighboring pores is tested for each dilation step. Assigning an interfacial tension to fluid-fluid interfaces and a contact angle to mineral-fluid-fluid three-phase contact lines allow the capillary pressure to be calculated for each dilatation step, i.e., for different saturations by the Young-Laplace equation. Comparison with experimental data shows close agreement with experimental drainage data, while there are significant discrepancies for imbibition reported [12].
The relative permeability is then simulated by solving the Navier-Stokes equation in the pore space connected by the individual fluid phase. This limits the two-phase flow to the connected phase volume. Ganglion dynamics, which can contribute to the mobility of the non-wetting phase, especially in the case of high wetting phase saturations, are therefore not considered [13, 14].

So far, the method has delivered good results for drainage, but showed limitations in terms of imbibition processes and uncertainty modeling. In particular, imbibition processes were limited, since only individual processes could be modelled, either forced (drainage) or spontaneous (imbibition) processes. The forced part of the imbibition was therefore not previously incorporated. In this work, we implement contact angle distributions in a deterministic and stochastic way. With this, we extend the imbibition process from purely spontaneous to forced imbibition, resulting in full range imbibition capillary pressure ($p_c(S_{WP})$) and relative permeability ($k_r(S_{WP})$) saturation functions. Furthermore, by introducing stochastic contact angle distributions, different fluid phase distributions are obtained, which allows for uncertainty analyses. To verify the simulation results, we check (a) whether the simulation results agree with experience from SCAL measurements, and (b) compare morphologically with experimentally derived results.

2 Numerical Methods and Developments

2.1. The Morphological Method

The morphological method (MM) is based on mathematical morphology and applies morphological operations to pore-scale rock images. It was originally developed by Matheron and Serra in 1964 in the frame of Serra's PhD thesis and later published in Serra et al. 1982 [15]. The basic operations dilation and erosion applied to the rock's pore structure enable the quantitative analysis of pore geometries with regard to the drainage displacement thresholds – the pore throats. The morphological identification of thresholds links the pore structure to capillarity and hence to fluid displacement physics. The mathematical fundamentals are discussed in detail in Hilpert and Miller's paper from 2001 [16]. Initially, the approach was limited to binary images, but can also be applied to greyscale images. A derivative, the pore MM, also known as maximum inscribed spheres [11], predicts the distribution of a wetting phase (WP) and a non-wetting phase (NWP) inside a porous medium.
In general, the MM predicts saturation changes on basis of geometrical rock properties and therefore intrinsically assumes that capillary forces are dominating compared to viscous forces, i.e., the capillary number is low. The method therefore distributes the two fluid phases by using morphological operations rather than solving partial differential equations. A criterion for a displacement event is the disconnection to the respective wetting and non-wetting reservoir attached to the system boundaries. For imbibition and drainage, we are (thoroughly) referring to the invasion of the WP and the NWP, respectively. The image operations change the topology of the fluid phases, which corresponds to the physical event of a capillary pressure change, where the extend of the dilation operation corresponds to the pore throat radius in the Young-Laplace equation. Figure 1 shows the displacement of the wetting phase (blue) by the non-wetting phase (green), for a solid phase with a single contact angle (grey) and multiple contact angle materials (grey and brown). The number of voxels dilated describes the radius r, which in a drainage process corresponds to the pore throat size. Different contact angles are introduced after Schulz, by scaling the dilation radius with the $cos(\theta)$, with θ being the contact angle [17]. This method slightly overestimates the actual contact angle and does not work for contact angles close to 90°.

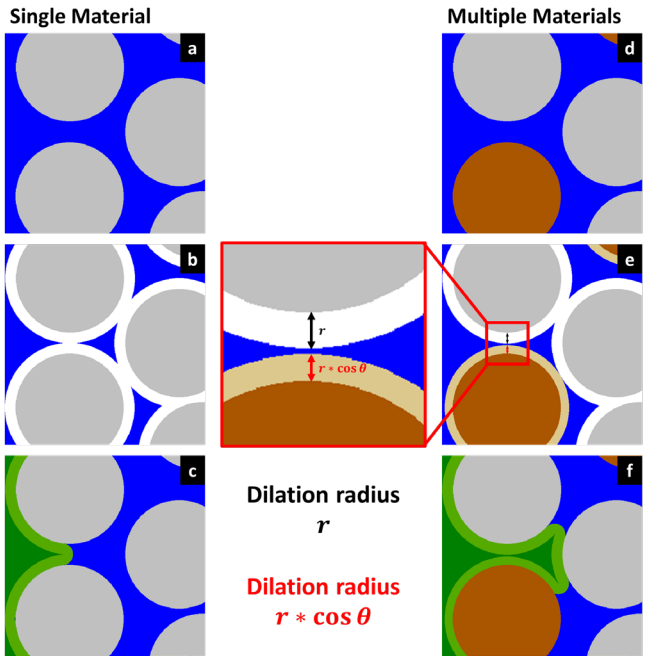

Fig. 1: *Simplified illustration of a drainage invasion step for a single contact angle material (a-c) and dual contact angle materials (d-f). Solid phases are colored grey and brown, the wetting phase is colored blue and the non-wetting phase green. Dilated volumes are indicated in the respective lighter color.*

2.2 Initial drainage and spontaneous imbibition implementations

A primary drainage is defined as the displacement of the wetting by the non-wetting phase. The process is described by a sequence of equilibrium steps, which mimic the invasion as a consequence of an applied differential pressure. A sequence of three operations corresponding to a single displacement event is shown in Figure 1. It illustrates a simplified 2D porous structure with circular grains in grey and the pore space filed with a wetting phase (blue). In the steps from images (a) to (b), grains are dilated to identify and close the narrowest pore throats. Defining the NWP reservoir on the left-hand side of the image, the invaded NWP is

connected to the NWP reservoir and recolored (dark green). In a next step, the NWP is dilated (light green) by the same voxel radius as the grains were dilated in the prior step. Since in a drainage process, the NW fluid invades first the larger pore throats, the invading fluid (green) phase cannot overcome the first pore throat which is indicated in image (c). The right-hand side of Figure 1 (d-f) shows that the approach can be modified by the introduction of a different mineral with a modified contact angle (brown). When applying multiple contact angles for the same scenario, the invading phase can overcome the same pore throat, since the dilation is scaled by $cos(\theta)$ (light brown), which results in different invasion pathways for the same applied pressure. In this process, the invading NWP must in every step be connected to the inlet phase, which is the NWP "reservoir", and the wetting phase to the outlet, the WP reservoir.
The algorithm of the above-described morphological drainage process consists of four steps:

1. Dilation of the grains into the WP pore space by a voxel radius r, which can be scaled by $\cos(\theta)$.
2. Recolor the pore space, which is connected to the NWP reservoir and label it as NWP.
3. Dilate the NWP by the initial (non-scaled) voxel radius from step one.
4. Recolor all WP, which is disconnected from the WP reservoir as residual. It will no longer be considered for further dilation steps.

The last step allows for a residual saturation and may be ignored when simulating mercury injection capillary pressure experiment [18]. Performing the drainage algorithm by gradually decreasing the radius r (number of voxels), results in a quasi-stationary invasion of the non-wetting phase. Scaling the dilation radius in step 1 by $\cos(\theta)$ alters the invasion pathway with regard to the wetting condition. When contacting non-wetting material, the pore space would immediately be populated by the approaching NWP. The interfacial tension is only accounted for in post-processing for calculating p_C and therefore results only in a up or down shift of the (resulting) p_C curves, but does not influence the (resulting) fluid distribution. A drainage process is either stopped when the WP is entirely disconnected from the outlet, or the dilation reaches a sub-voxel value.
The basic algorithm for drainage can be modified to simulate imbibition processes, by interchanging step 2 and 3. An imbibition front stops, when either the NWP is disconnected from the NWP reservoir or the dilation radius exceeds the size of the largest pores, i.e., allowing no fluid phase changes anymore or non-wetting material cannot be bypassed by the WP anymore, acting as a barrier.

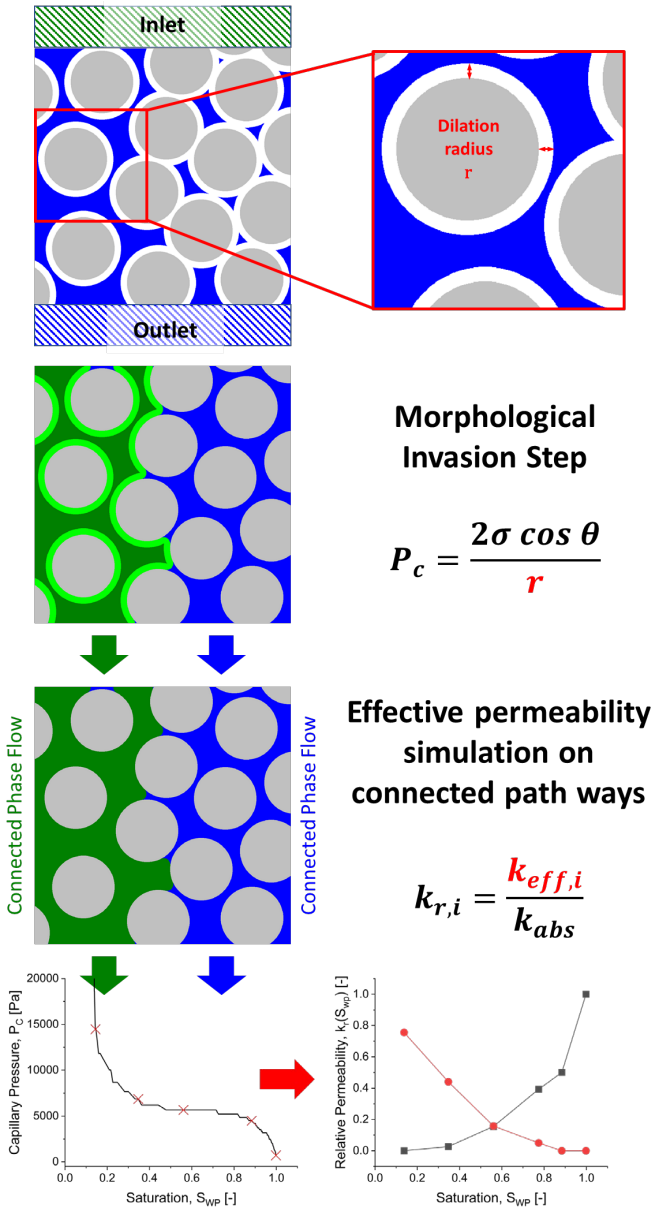

Fig. 2: Simplified 2D illustrated phase population by the MM, resulting in two connected pathways for the given saturation state. The bottom image, shows the simulated $k_r(S_{WP})$ on basis of individual saturation steps acquired from a capillary pressure drainage simulation on a Berea sandstone.

2.3 Simulation of effective permeability

The $p_C(S_{WP})$ saturation function is a direct result of the MM, i.e., a purely structural property. Furthermore, the MM delivers the fluid distribution in the pore space for each simulated saturation state and hence, information on the connectivity of both phases. The MM, however, does not deliver permeability and $k_r(S_{WP})$ directly. While the absolute permeability (K) is simulated by solving the Stokes equation on the total pore space, assuming single phase flow for a small constant pressure drop in flow direction ($\Delta p = 0.02\ Pa$) and periodic boundary conditions in the tangential direction. Since we are having very slow flows, due to the small pressure drop, we solve the Stokes instead of the Navier-Stokes equation as it delivers the same results while

being computationally less demanding. The effective permeability ($k_r(S_{WP})/K$) is simulated for each fluid phase separately, considering the respective connected pathways only. This means that $k_r(S_{WP})$ simulations consider the respective other phase as immobile, i.e., all internal boundaries as rigid and fixed. Furthermore, $k_r(S_{WP})$ can only be calculated in cases the respective fluid phase is connected throughout the simulation domain at the given saturation state, otherwise it is zero. A snap-off event can therefore lead to the loss of phase conductivity, while the phase is still accessible for a displacement event, as it is connected to the outlet.

2.4 Limitations of the initial implementation

As described earlier, the MM is based on geometric operations on the digital rock structures and is therefore entirely governed by the porous structure and, if present, residual fluid phases. This describes the nature of a primary drainage process quite well, as the non-wetting phase intrusion is restricted by the pore throat radii, which inversely scale to the capillary pressures. However, processes like imbibition are partly spontaneous and rather driven by interfacial properties like wetting state and contact-angle distribution. How well does the MM capture the physical process? For a single contact angle, the invading fluid always takes the same pathway through the porous domain independent of the contact angle. This means that a contact angle variation will not alter the invasion sequence and the resulting fluid distribution and is therefore not changing the relative permeability curves.

The implementation of multiple contact angles was addressed by Schulz et al. [17]. Hereby the invasion process is altered by scaling the dilation radii with $cos(\theta)$, however limiting the system to contact angles below or above 90° – for contact angles in a range between 60° and 120° the simulations are likely to fail. The introduction of multiple contact angles allows for variating displacement pathways.

After all, the imbibition process as given above is still limited to the spontaneous part of the capillary pressure curve, i.e., to the positive P_C range, which results in a limited saturation range. So far one of the stopping criteria is a disconnection of the NWP from the NWP reservoir. We typically describe the flow in a single direction and therefore assign the lateral boundary conditions as periodic, while the inlet as connected to an WP reservoir and the outlet connected to the NWP reservoir. Hence, the invasion process can result in an early snap-off of the NWP, while leaving a larger part of the saturation as residual. This results in a drastic reduction of the NWP effective permeabilities, respectively increase for the WP.

2.5 Full-scale imbibition

While the drainage process is defined as the invasion of the non-wetting phase, i.e., indicated by an entirely positive capillary pressure, imbibition processes can show an early saturation range of positive and a late saturation range of negative capillary pressure. A negative capillary pressure indicates a forced process, which actually can be understood as drainage process. Therefore, in order to simulate the full saturation range with the pore MM, we first couple the imbibition process with a subsequent drainage process.

The stopping criteria of the spontaneous imbibition (SI) process is the disconnection of the NWP from the outlet – the NWP is trapped and cannot be displaced neither by an imbibition nor by a drainage algorithm. In order to switch from a spontaneous to a forced process, a non-wetting material must be introduced, which prevents access of parts of the pore space by the spontaneous process. This may be physically correct, because it reflects the meaning of a negative capillary pressure. A straightforward implementation is the introduction of non-wetting material before the start of the SI modelling. Depending on the topology and volume of non-wetting material introduced, the SI stops at different saturation stages. In this work, the non-wetting material is introduced in two alternative ways:

1. Introduction of non-wetting material on basis of stochastic field before the drainage process. This ensures that the non-wetting material is in contact with the NWP at the end of the drainage process.
2. Introduction of non-wetting material at the end of the drainage process in NWP filled pores only, prioritizing the biggest pores first.

In the stochastic approach the volumetric percentage and region size considered for the stochastic field are defined. The material is then implemented on basis of an isotropic gaussian random field. Figure 3 shows the exemplary implementation of non-wetting material with two different region sizes. In both cases the same random seed was chosen, whereas one region size is smaller and the other bigger than the average grain size visible. Depending on the region size and solid volume percentage (SVP) considered, unavoidably the introduced material can be interconnected throughout the structure. The volume percentage of material changed equals the surface area percentage between the pore and solid materials with minor deviations.

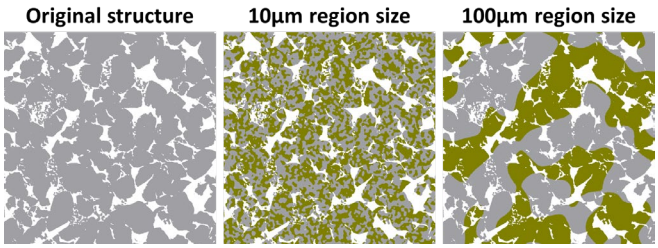

Fig. 3: *A second material introduced on basis of a stochastic field in a digital twin (left) of the size of 1472x1472 µm. The yellow material corresponds in both cases to a solid volume percentage (SVP) of 50% of the structure, with different region sizes of 10µm (middle) and 100µm (right).*

The deterministic approach is based on the natural process of a wettability alteration during an ageing process, where mineral surfaces in contact with the NWP can change their initial wetting state [19–21]. It applies an algorithm at the end of a drainage process, analyzing the pore size distribution and introducing non-wetting material in the biggest pores first, only at contacts of the mineral and NWP. In the algorithm we define the volume of pores considered for the

implementation. The volume considered does not equal the surface area, as only a part of the pore material is changed. Figure 4 illustrates the algorithm on a simplified structure. The different pore sizes are displayed as volume field scaled by a hue-saturation-lightness color legend, where blue represents the smallest and red the biggest pores. In the second illustration the pore space, which is considered by the algorithm is marked as red. The pore space considered is a user input so far and can be varied between 1% to 99%. The last two images show the resulting material changes, where only material in contact with the previous marked pores is considered, while prioritizing the material in the bigger pores. This algorithm has the advantage that different non-wetting contact angles can be introduced at the end of the drainage.

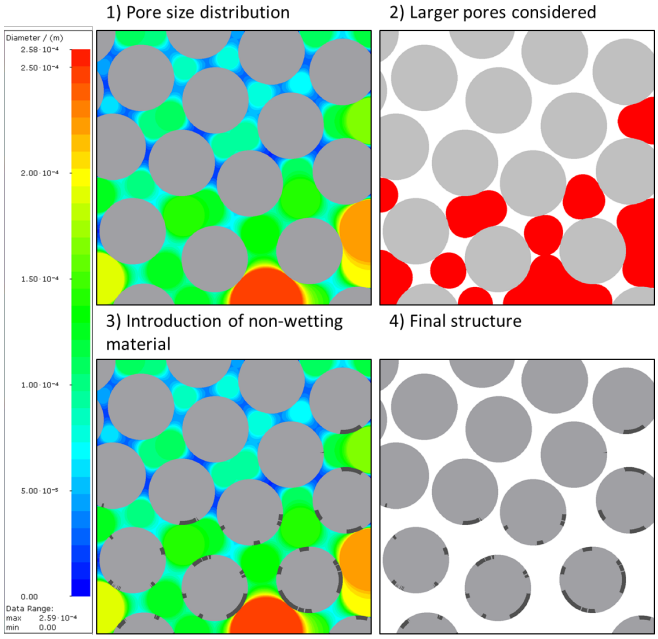

Fig. 4: *Simplified illustration of the deterministic algorithm for introduction of non-wetting material, assuming the pore space is entirely filled with the NWP. After the pore-throat size distribution (1), 50% of the largest pores (2) are considered for the implementation of non-wetting material, resulting in a change of the structure (4). In image (3) it can be seen that bigger pores are prioritized for the implementation of the new material. The structure has a size of 1000x1000 voxels and resolution of (1 µm)³/voxel.*

The forced imbibition (FI) part is then modelled with the drainage algorithm where the contact angles and the role of the phases are inverted. This means that a non-wetting contact angle is considered to be wetting (i.e. $180°-\alpha$) for the FI drainage process, while swapping the role of the WP and NWP. This corresponds to a turnover of the menisci between the WP and NWP at the transition from the spontaneous to the forced displacement process.

2.6 Comparison to experimental data

A steady-state experimental data set [12] was used as reference for benchmarking. The data set consists of a time series of pore-scale-resolved fluid distributions on which NWP and WP effective permeability can be simulated and directly compared to the respective results from the MM. This benchmark was carried out by Berg et al. and is repeated in the present work with and without the described modifications in the MM. While in the earlier study relative permeability simulated on the numerical and experimental fluid distributions show a substantial mismatch, with the embedded innovations, a much closer match could be achieved as discussed in the result part.

2.7 Simulation input

The uncertainty analysis for the contact angle distributions was performed on a Berea Sandstone with the dimensions of 800x800x800 voxels and a voxel size of 1.84 µm. The digital rock sample has a resolved porosity of 19.6% and a simulated permeability of 780 mD.

The synchrotron experiment by Berg et al. was conducted on a Gildehauser sandstone, with an average resolved porosity of 20% and a permeability of 1.5±0.3 D. For the comparison to simulations on the experimentally derived fluid distributions, the pre-segmented dataset from the digital rocks portal were used [22]. The digital twin has a resolution of (4.4 µm)^3/voxel and consists of a cylindrical domain with the dimension of 830x830x566 voxels. The digital twin has a porosity of 20.3% and a simulated permeability of 1.55 D.

3 Results

In order to test the innovations introduced with this work, we use the new degrees of freedom to define the wetting state and simulate different scenarios. First, we simulate capillary pressure curves on a digital twin for Berea sandstone. With this, we compare the results for the stochastic and deterministic implementation and for different wetting states in order to assess the trends in the $p_c(S_{WP})$ on a physical basis. Second, we compare the new approaches with experiments by simulating $k_r(S_{WP})$ for experimentally and morphologically determined fluid distributions, while varying the simulated wetting states.

3.1 Full-scale imbibition and introduction of non-wetting material

In the previous section, we introduced two principally different algorithms for the implementation of non-wetting material, a stochastic and a deterministic algorithm. For the stochastic algorithm, the non-wetting material is introduced prior to the drainage process, which ensures that the non-wetting pores are filled with the NWP at connate WP saturation. With regard to the subsequent imbibition process, the higher the SVP of the non-wetting region the earlier the spontaneous imbibition is stopped and the bigger is the contribution of the forced part to the total imbibition process. Furthermore, the region size chosen is critical as it influences the drainage and imbibition. In Figure 5 we can observe these changes, where an increasing SVP and decreasing region size result in a more non-wetting state of the system. The dark yellow symbols, which partly overlay with the newly modelled data sets, show the results of the initial drainage and spontaneous imbibition implementation. In this case, there is only one wetting contact angle assigned, and therefore only spontaneous imbibition can be modelled. To make the systems comparable for all combinations the same contact

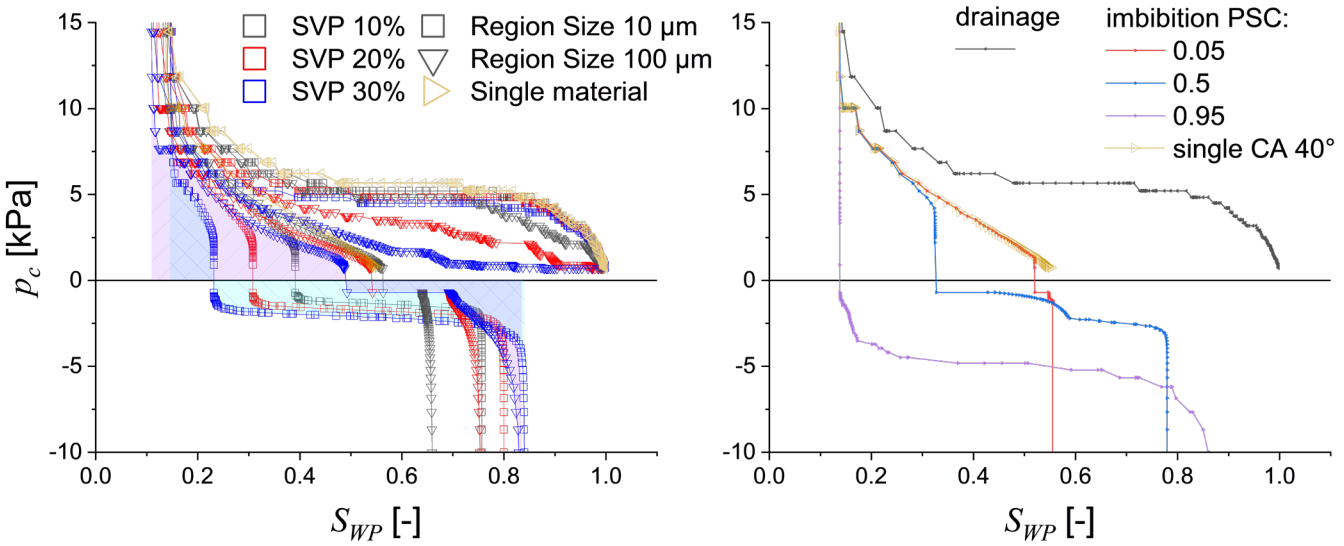

Fig. 5: *Data modelled with the stochastic approach: Influence of the region size and solid volume percentage (SVP) on the drainage and imbibition curve (left). The marked areas underneath the curve indicate the wetting conditions of the SVP 30% case for a region size of 10µm (cyan) and 100µm (magenta), indicating non-wetting and wetting conditions respectively, when comparing the positive and negative areas below the curves. The yellow line represents the single material base case, without a forced imbibition. Data modelled with the deterministic approach: Influence of the pore space considered (PSC) on the imbibition curve (right).*

Three different non-wetting volume changes (10%, 20%, 30%) with two different region sizes (10 and 100 μm) were modelled, resulting in additional 6 scenarios. While the residual WP saturation is rather unaffected, the residual NWP saturation decreases with increasing SVP and decreasing region size, which is coherent with the proportion of spontaneous to forced imbibition. An increasing volumetric proportion of non-wetting material results in a more non-wetting trend. The region size on the other hand displays the opposite, where a decrease of the region size leads to an earlier inhibition of the spontaneous imbibition. This is a result of the spatial distribution of non-wetting material, even though the surface area of non-wetting material is approximately the same for both region sizes, we do have more pores which are affected by non-wetting material. Consequently, the available pore space for the invasion during the spontaneous process is reduced. The effect of the region size, respectively the contact angle spatial distribution is large. It can make the overall system water wet or oil wet, which is directly recognized by comparing the positive and negative areas under the curve (indicated by the shaded areas for the SVP 30% cases in Figure 5), which links directly to the work the system does to the environment (spontaneous and positive) and the work the environment does to the system (forced and negative) – the ratio corresponds to the wettability index. When taking the logarithm of that ratio, similar to the U.S. Bureau of Mines (USBM) wettability index, positive values indicate a wetting behavior, as the spontaneous work is larger than the forced work and vice-versa. This makes the 30% SVP system with the 10 μm region size non-wetting and the one with 100 μm wetting, as indicated by the indices of -0.51 and 0.34 respectively.

It is worth mentioning that also the drainage curves are affected. For the smaller region sizes, more work is required to desaturate the system, if the region size is smaller. The reason may be that with larger region sizes, some pores are wetting to the NWP and therefore a fraction of the volume can be invaded by the NWP without effort.

In the deterministic approach the non-wetting material is implemented at the end of the drainage process, which leaves the drainage process itself unaffected. Therefore, unlike in the stochastic approach, all imbibition scenarios start form the same point (drainage endpoint). Despite the substantial differences of both algorithms, the trends are similar with regards to the forced imbibition part and the residual NWP saturation. However, as discussed above, the exact NWP distribution after drainage determines the non-wetting material distribution. The right panel of Figure 5 shows the results, when assigning non-wetting material, while considering 5%, 50% and 95% of the entire pore space; the more pore space is considered for turning to non-wetting material, the more the systems behaves non-wetting. This is displayed by lower residual NWP saturations and larger areas under the negative p_c branch. When considering almost the entire pore space (the 95% case in Figure 5), we do not have any spontaneous imbibition, as the WP front does not have any available space for advancing spontaneously, since it is immediately confronted with non-wetting material. For systems with low pore volume considered, the spontaneous imbibition follows the original trend, as only a small portion of the system is unavailable for the invasion sequence. Generally, both algorithms display similar trends with an increasing volume of non-wetting material introduced.

A difference of the imbibition p_c curves simulated with the MM and laboratory p_c curves, is the abrupt p_c drop at the transition from the spontaneous to the forced part of the curves across the $p_c = 0$ condition. We believe that this jump is physically correct and is a result of (a) a discrete contact angle distribution, and (b) a result of the finite size of the digital twin. We anticipate at this point that it has no influence on the simulated relative permeabilities:

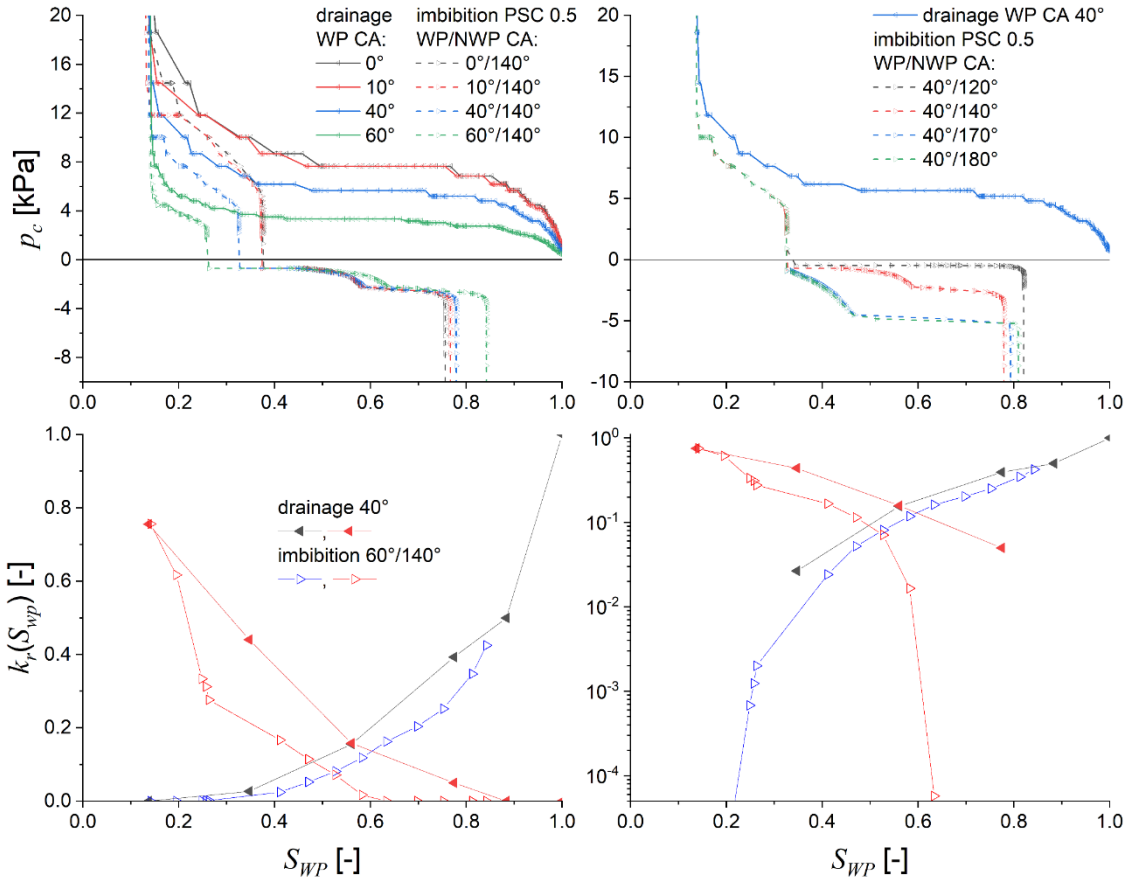

Fig. 6: *Capillary pressure curves (top) when applying the deterministic modelling approach, while considering 50% of the pore space for the non-wetting material implementation. Sensitivities to the wetting (left) and non-wetting (right) contact angles. The relative permeability curves show the effective extension of the connectivity of the wetting and non-wetting phase on a linear (left) and logarithmic (right) scale beyond the spontaneous imbibition*

At the point at which Imbibition changes from spontaneous to forced, all the pore space that can be spontaneously invaded is invaded. At that point, the interfacial curvature locally flips from concave (from the perspective of the wetting phase) to convex with only a neglectable saturation change. During the flip, the system crosses the $p_c = 0$ condition. Therefore, this discontinuity may be mitigated (a) by a continuous contact angle distribution, and (b) by investigating macroscopic system sizes as for classical p_c measurements. With respect to (a) it depends very much on the reason for contact angle variation – is it due to mineral-to-mineral variation or due to aging, or both. In all cases, the contact angle distribution may be discontinuous. With regards to (b), the MM as well as p_c measurements are based on fluid invasion processes. We assume that locally one process dominates, i.e., spontaneous or forced imbibition. However, for larger sample domains it may be that at a given time at different positions, there are slightly different saturation states. This would smoothen experimentally derived p_c curves for an average saturation state.

3.2 Sensitivity to the contact angle

To study the sensitivities to the implemented contact angles on imbibition p_c and k_r, the deterministic approach is used, where the material is implemented at the end of the drainage process. This guarantees a better comparability, as the drainage process is not affected by the non-wetting contact angle.

In contrast to the initial implementation, two contact angles are assigned, resulting in a material distribution with the initially assigned wetting contact angle and with a modified contact angle. The modified areas are those prioritized by the primary drainage process to be in contact with the non-wetting phase material. A certain volume percentage of the prioritized area was then assigned to non-wetting contact angles. While drainage is determined by the wetting contact angle only, imbibition is sensitive to both. Unless otherwise stated and for comparability, the chosen pore space considered, 50%, is the same for all simulations. The left panel of Figure 6 shows the results by variation of the WP contact angle by leaving the NWP contact angle constant. Both curves, drainage and imbibition are affected. With increasing WP contact angle, less pressure is required for the NWP to enter the pore space – the p_c curve is lowering. Referring to imbibition, a contact angle increase lowers the saturation range for the SI and decreases the residual NWP saturation. These are clear indications of a less wetting behavior of the system, which is expected when applying a higher contact angle to the wetting phase. Furthermore, it can be observed that the shape of the forced imbibition curve is not influenced as it is governed entirely by the non-wetting contact angle. The earlier the forced imbibition is started, the larger the overall saturation range. This behavior is expected

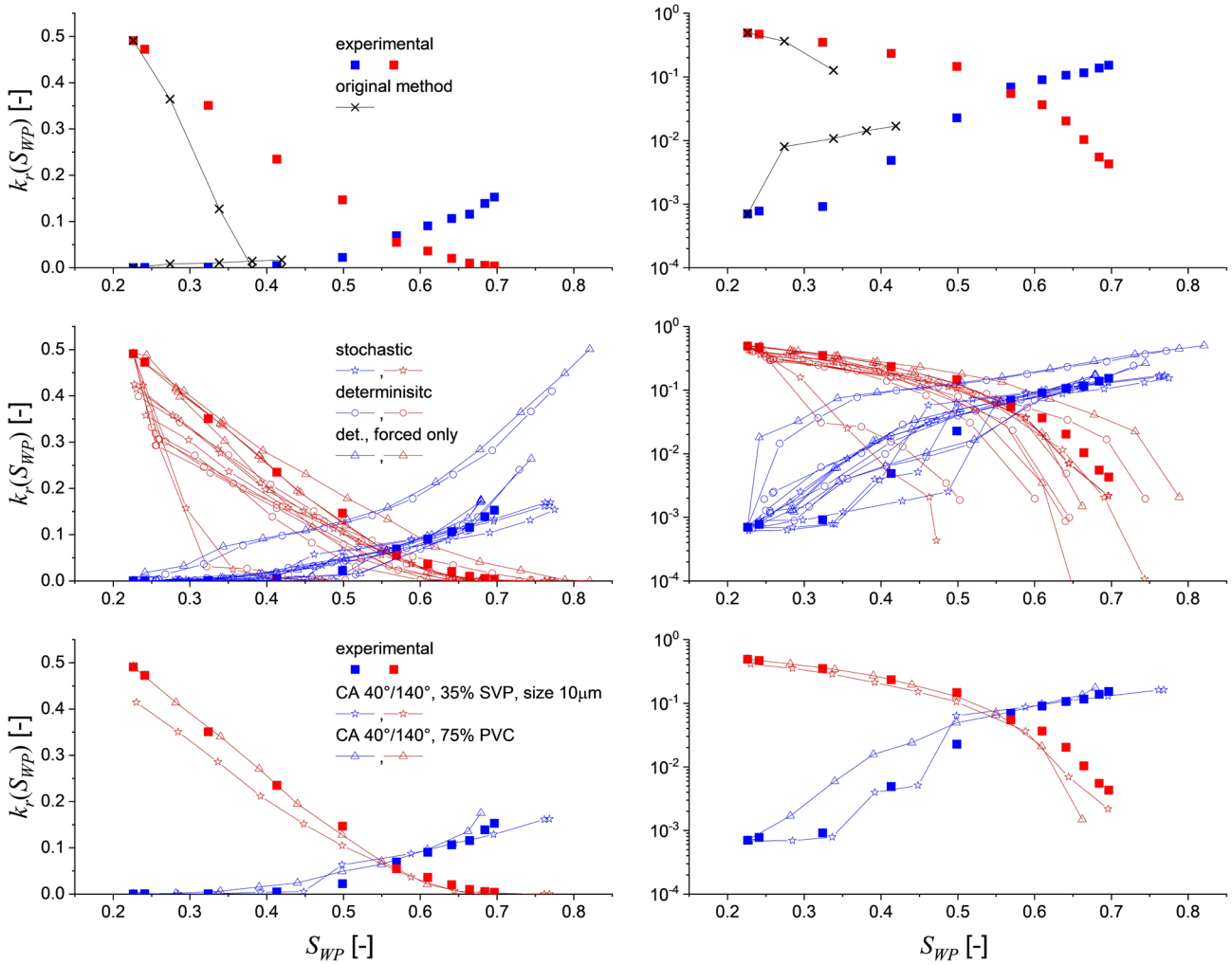

Fig. 7: *Relative permeability curves on a linear (left) and logarithmic (right) scale. The experimental data is displayed by solid squares (■). In the top panel the experimental data is compared with the original populated models. The middle shows a cloud of relative permeabilities modelled for different wetting and non-wetting contact angle combinations. The last panel shows the best matches for the deterministic and stochastic modelling approach.*

from SCAL experience and is also reflected in the subsequent simulation of the relative permeability curves.

The right panel of Figure 6 shows the influence of the non-wetting contact angle. As the wetting contact angle is kept constant, only the forced imbibition is influenced. It can be observed that not only residual saturations, but also the shape of the curve is changing. Except for 120°, an increasing non-wetting contact angle results in a lower residual NWP saturation. However, the effects are minor compared to those of the wetting contact angle, which effect both parts of the curve. As seen in Figure 6 not only the cross-over at $p_c = 0$ but also the saturation endpoints are changing, which is resulting from the nature of the spontaneous and forced imbibition algorithms. Since the forced imbibition is modelled like a drainage process, the residual saturations are governed by the preexisting fluid phase distributions and the pore throat structure of the medium. As the starting point, namely the end of the SI is the same for all configurations the curves are only influenced by the scaling with the $cos(\theta)$ during the dilation process. This results in slightly altered pathways, with similar final states.

Generally, we observe that the trends of the capillary pressure curves show physical trends with regard to contact angles and associated wettability index. The most influential parameter has proven to be the way, the non-wetting material is introduced as displayed in Figure 5, where here the size and volume are of essence, as is acts as stopping criteria for the advancing SI front.

3.3 Relative permeabilities from morphological vs. experimental fluid distributions

A previous study by Berg et al. [12] has shown that imbibition relative permeability curves simulated morphologically and experimentally determined fluid distributions greatly disagree. In this section, we make the same comparison with the modified morphological approach and the respective extended imbibition saturation range. Furthermore, in the modified morphological approach, there are tuning parameters to (a) fit the numerical to the experimental results, and (b) to determine an uncertainty range. Since the experimental data refer to a water-oil displacement, we refer in this section to water and oil instead of WP and the NWP, without losing generality. We predominantly applied the deterministic algorithm to investigate the sensitivity of the

relative permeabilities with respect to different wetting states of the system. To minimize numerical capillary end effects, which can highly influence relative permeability, we mirrored the domain in flow direction. For the flow simulations, we cropped the domain back to its original size. The procedure proved to have only minor influences on the saturations, but improved the connectivity of the phases as a premature disconnection at the end of the domain is avoided.

As a starting point for the imbibition simulations, the experimental fluid phase distribution was used at connate water saturation of $S_{w,c} = 0.21$. The experimental residual oil saturation ($S_{o,r} = 0.29$) served as a reference end point to choose the right parameters for the algorithm. The imbibition simulations were performed considering 75% of the pore space for conversion, which resulted in a residual oil saturation ranging from 0.25 to 0.35 for non-wetting material contact angle of 180° and 140° respectively. With the initial implementations already shown in the study of Berg et al. [12] a $S_w = 0.41$ was reached at the end of the spontaneous imbibition process. In the top row of Figure 7, we show the experimental relative permeability curves in comparison with the initial morphological modelling approach. When applying the new algorithm, we reduce the spontaneous imbibition saturation ranges to between 0.25 to 0.32 depending on the chosen water-wet contact angle. These are only minor saturation changes with respect to the starting saturation, which is a result of the relatively high amount of pore space considered for the implementation of the non-wetting material. In the middle row of Figure 7 the range of resulting relative permeability curves are plotted, showing that we successfully extended the saturation range while reducing the offset to the experimental data.

The water wetting contact angle mainly influences the oil relative permeability, while the non-wetting contact angle influences both. The lower the water wetting contact angle, the lower the oil relative permeability is, this effect is very prominent especially at the early stage of the imbibition. Since the reduced connectivity of the oil comes from the spontaneous imbibition, the effect is more prominent for strongly wetting contact angles around $\theta = 0°$. This results from the trends shown in Figure 6, where the SI part of the curve is larger for low contact angles, respectively the forced part smaller. This is a consequence of NWP clusters, which have been disconnected during the SI process and will not be reconnected during the forced imbibition process. Therefore, we get more of a water wet trend, with regard to the oil relative permeability, the less is modelled spontaneously. Especially since the NWP cannot be reconnected during any further displacement events. On the first view this may appear counter intuitive. On the other hand, in a flow experiment, water may invade with a higher rate than being spontaneous, i.e., imbibition may be forced.

The middle row in Figure 7 shows the simulation results for different contact angle combinations. In the different relative permeability realizations of our system, the outliers from the experimental data are from simulations using contact angle of 120° for the NWP, where we have already seen in the p_c curves that this contact angle does not act in accordance with the other trends. Furthermore, one of the datasets is modelled with a large region size, which results in a strong SI and therefore a mismatch to the experimental data.

The best matches were achieved, as shown at the bottom of Figure 7, when modelling the imbibition process by a forced imbibition only. For both, the stochastic and deterministic implementation, avoiding extreme contact angles, i.e., contact angles close to 0°, 90° and 180°, proved to work best. To make sure the deterministic and stochastic approach are comparable, the same volume of introduced non-wetting material and a small region size (10 µm) for the later was chosen. Even though the residual saturations for both approaches differ, the trend and results for the $k_r(S_w)$ are similar. This could be an indication that for the displacement of the non-wetting phase the pore throat radii, hence the pore structure itself is more dominating than the wetting conditions implied.

Using the degrees of freedom as discussed above, leads to a cloud of relative permeability curves, which represents an uncertainty interval with respect to the wetting condition. This data can now be compared to the simulation results on the experimental fluid distribution by Berg et al. The experiments were performed under steady-state conditions, where the system was imaged at different fractional flow conditions. Since for each fractional flow step a steady state was reached, the flow must correspond to a process forced by injection. In addition, Berg et al. observed water film swelling by saturation changes at the beginning of imbibition, without significant displacement events taking place. Assuming this film swelling represent the spontaneous imbibition process, it would only account for a limited saturation range, whereas further displacement is connected to a forced displacement. This would correlate with the large number of pores where non-wetting material was introduced (PSC = 75%), and hence an only small SI range to match the experiment.

4 Summary and Conclusion

We successfully combined morphological algorithms for spontaneous and forced processes to describe the full-range imbibition capillary pressure and relative permeability curves. For this, distributions of wetting and non-wetting regions were introduced. With this, a premature stopping criterium for the spontaneous process was introduced, maintaining the connectivity of both phases at the end of the spontaneous process. As both phases are still connected, a subsequent forced imbibition process can be modelled by using the drainage MM.

For the implementation of the non-wetting regions, two approaches were developed, a deterministic and a stochastic approach. Capillary pressure curves were modelled for both approaches. By varying the nonwetting-region sizes and distributions and the contact angles and their combinations, we could show that the p_c follows physical trends and SCAL experiences [19,21,23-25].

Relative permeability curves were then calculated by solving the Stokes equations on the connected pathways for different saturation states. Varying the wettability-related parameters

results in an uncertainty interval that may be used for stochastic reservoir modeling. Relative permeability was predominantly calculated on a data set by Berg et al., which allowed a comparison between the original MM, the MM as modified in the frame of this work, and experimentally determined fluid distributions. A good match between morphological and experimental data could be achieved by avoiding strong wetting conditions, while modelling the imbibition process with a forced imbibition only. This is potentially due to the actual nature of the imbibition process under injection conditions, which may rather be forced than spontaneous.

In summary, with the made modifications, the morphological method can be used to model imbibition over the full saturation scale. We were able to demonstrate realistic physical trends and to deliver realistic results in comparison to pore-scale experiments. The wettability-related parameters can be used for uncertainty modeling and to match morphological to experimental results. However, we are still lacking the possibility to implement true neutral wetting conditions, as simulations with contact angles between 60° and 120° fail, or result in saturation end points opposing the actual physical trends. Being able to model contact angles in this interval would mitigate or even remove the sharp transitions between spontaneous and forced imbibition. Further investigation is needed to explain the best match by assuming a pure forced ambition. This may be a result of potentially high viscous forces during the injection experiment, which may make the imbibition forced across the full saturation scale. This is the definition of a drainage process. The remaining questions are how to narrow down the input parameters in cases where no experimental data are available, and to a certain extent their physical interpretation of the best matches.

References

[1] C. Pan, M. Hilpert, and C. T. Miller, “Lattice-Boltzmann simulation of two-phase flow in porous media,” *Water Resour. Res.*, vol. 40, no. 1, 2004, doi: 10.1029/2003WR002120.

[2] C. Chukwudozie and M. Tyagi, “Pore scale inertial flow simulations in 3-D smooth and rough sphere packs using lattice Boltzmann method,” *AIChE J.*, vol. 59, no. 12, pp. 4858–4870, 2013, doi: 10.1002/aic.14232.

[3] E. S. Boek, I. Zacharoudiou, F. Gray, S. M. Shah, J. P. Crawshaw, and J. Yang, “Multiphase-Flow and Reactive-Transport Validation Studies at the Pore Scale by Use of Lattice Boltzmann Computer Simulations,” *SPE Journal*, vol. 22, no. 03, pp. 940–949, 2017, doi: 10.2118/170941-PA.

[4] F. O. Alpak, S. Berg, and I. Zacharoudiou, “Prediction of fluid topology and relative permeability in imbibition in sandstone rock by direct numerical simulation,” *Advances in Water Resources*, vol. 122, pp. 49–59, 2018, doi: 10.1016/j.advwatres.2018.09.001.

[5] M. J. Blunt, “Flow in porous media — pore-network models and multiphase flow,” *Current Opinion in Colloid & Interface Science*, vol. 6, no. 3, pp. 197–207, 2001, doi: 10.1016/S1359-0294(01)00084-X.

[6] B. Zhao *et al.,* “Comprehensive comparison of pore-scale models for multiphase flow in porous media,” *Proceedings of the National Academy of Sciences of the United States of America*, vol. 116, no. 28, pp. 13799–13806, 2019, doi: 10.1073/pnas.1901619116.

[7] V. Joekar-Niasar and S. Majid Hassanizadeh, “Effect of fluids properties on non-equilibrium capillarity effects: Dynamic pore-network modeling,” *International Journal of Multiphase Flow*, vol. 37, no. 2, pp. 198–214, 2011, doi: 10.1016/j.ijmultiphaseflow.2010.09.007.

[8] H. Dong and M. J. Blunt, “Pore-network extraction from micro-computerized-tomography images,” *Phys. Rev. E*, vol. 80, 3 Pt 2, p. 36307, 2009, doi: 10.1103/PhysRevE.80.036307.

[9] J. T. Gostick, “Versatile and efficient pore network extraction method using marker-based watershed segmentation,” *Physical review. E*, vol. 96, 2-1, p. 23307, 2017, doi: 10.1103/PhysRevE.96.023307.

[10] W. B. Lindquist and A. Venkatarangan, “Investigating 3D geometry of porous media from high resolution images,” *Physics and Chemistry of the Earth, Part A: Solid Earth and Geodesy*, vol. 24, no. 7, pp. 593–599, 1999, doi: 10.1016/S1464-1895(99)00085-X.

[11] D. Silin and T. Patzek, “Pore space morphology analysis using maximal inscribed spheres,” *Physica A: Statistical Mechanics and its Applications*, vol. 371, no. 2, pp. 336–360, 2006, doi: 10.1016/j.physa.2006.04.048.

[12] S. Berg *et al.,* “Connected pathway relative permeability from pore-scale imaging of imbibition,” *Advances in Water Resources*, vol. 90, pp. 24–35, 2016, doi: 10.1016/j.advwatres.2016.01.010.

[13] M. Rücker *et al.,* “From connected pathway flow to ganglion dynamics,” *Geophys. Res. Lett.*, vol. 42, no. 10, pp. 3888–3894, 2015, doi: 10.1002/2015GL064007.

[14] R. T. Armstrong, J. E. McClure, M. A. Berrill, M. Rücker, S. Schlüter, and S. Berg, “Beyond Darcy's law: The role of phase topology and ganglion dynamics for two-fluid flow,” *Physical review. E*, vol. 94, 4-1, p. 43113, 2016, doi: 10.1103/PhysRevE.94.043113.

[15] J. P. Serra, J. Serra, and N. Cressie, *Image Analysis and Mathematical Morphology*: Academic Press, 1982. [Online]. Available: https://books.google.at/books?id=6pZTAAAAYAAJ

[16] M. Hilpert and C. T. Miller, “Pore-morphology-based simulation of drainage in totally wetting porous media,” *Advances in Water Resources*, vol. 24, 3-4, pp. 243–255, 2001, doi: 10.1016/S0309-1708(00)00056-7.

[17] V. P. Schulz, E. A. Wargo, and E. C. Kumbur, “Pore-Morphology-Based Simulation of Drainage in Porous Media Featuring a Locally Variable Contact Angle,” *Transport in Porous Media*, vol. 107, no. 1, pp. 13–25, 2015, doi: 10.1007/s11242-014-0422-4.

[18] B. Ahrenholz *et al.,* "Prediction of capillary hysteresis in a porous material using lattice-Boltzmann methods and comparison to experimental data and a morphological pore network model," *Advances in Water Resources*, vol. 31, no. 9, pp. 1151–1173, 2008, doi: 10.1016/j.advwatres.2008.03.009.

[19] M. Rücker *et al.,* "Relationship between wetting and capillary pressure in a crude oil/brine/rock system: From nano-scale to core-scale," *Journal of colloid and interface science*, vol. 562, pp. 159–169, 2020, doi: 10.1016/j.jcis.2019.11.086.

[20] G. J. Hirasaki, J. A. Rohan, S. T. Dubey, and H. Niko, "Wettability Evaluation During Restored-State Core Analysis," in *All Days*, New Orleans, Louisiana, 09231990.

[21] Wael Abdallah, Jill S. Buckley, Andrew Carnegie, John Edwars, Bernd Herold, Edmund Fordham, Arne Graue, Tarek Habashy, Nikita Seleznev, Claude Sighner, Hassan Hussain, Bernhard Montaron, Murtaza Ziauddin, "Fundamentals of Wettability," pp. 44–61, 2007.

[22] Steffen Berg, Ryan Armstrong, and Andreas Weigmann, "Gildehauser Sandstone," 2018. https://doi.org/10.17612/p7ww95

[23] W. Anderson, "Wettability Literature Survey- Part 2: Wettability Measurement," *Journal of Petroleum Technology*, vol. 38, no. 11, pp. 1246–1262, 1986, doi: 10.2118/13933-PA.

[24] X. Zhou, N. R. Morrow, and S. Ma, "Interrelationship of Wettability, Initial Water Saturation, Aging Time, and Oil Recovery by Spontaneous Imbibition and Waterflooding," SPE Journal, vol. 5, no. 02, pp. 199–207, 2000, doi: 10.2118/62507-PA.

[25] S. Zou and R. T. Armstrong, "Multiphase Flow Under Heterogeneous Wettability Conditions Studied by Special Core Analysis and Pore-Scale Imaging," *SPE Journal*, vol. 24, no. 03, pp. 1234–1247, 2019, doi: 10.2118/195577-PA.